nature communications

Article

https://doi.org/10.1038/s41467-026-70759-8

Molecular mechanism of menthol-induced TRPV5 channel inhibition

Received: 21 April 2025

Accepted: 4 March 2026

Published online: 18 March 2026

Check for updates

Angélica Méndez-Reséndiz[1,5], José J. De Jesús-Pérez[2,3,5], Gisela E. Rangel-Yescas[1], Tamara Rosenbaum[4], Vera Moiseenkova-Bell[2,3] ✉ & León D. Islas[1] ✉

TRPV5 channels play a critical role in calcium homeostasis and are implicated in various pathophysiological conditions. Here, we demonstrate that the monoterpene menthol, commonly used for pain and inflammation management, is an inhibitor of TRPV5. Electrophysiology experiments reveal that menthol blocks ion conduction through a slow blocker mechanism. Using single-particle cryo-EM, we determine the structure of menthol-bound TRPV5, which shows menthol interacting with W583, a residue previously implicated in channel permeation, gating and binding of endogenous modulators. These findings expand the repertoire of TRPV5 modulators and suggest that menthol could serve as a scaffold for developing channel-targeting modulators.

TRP channels are important regulators of cation transport in a myriad of organisms and tissues. Vanilloid TRP channels consist of subtypes TRPV1-6 and constitute one of the most diverse subfamilies, including members activated by temperature, lipids, and natural compounds that participate in various important physiological and pathophysiological processes. Most TRPV channels exert their actions through calcium (Ca^{2+}) signaling or the regulation of Ca^{2+} homeostasis[1].

Among the TRPV channels, TRPV5 has one of the highest permeabilities for Ca^{2+} ions over monovalent cations, with a relative Ca^{2+} to Na^{+} permeability ~100[2], a property it shares with its homolog protein, TRPV6, with 70% amino acid sequence homology between both proteins[3,4]. These channels are mainly found in Ca^{2+}-absorbing epithelia, such as kidney and intestinal tissues, where their main function is the reabsorption of Ca^{2+}. TRPV5 is primarily expressed in kidney epithelial cells, specifically localized to the apical membrane of cells of the distal convoluted tubules (DCT) and connecting tubules (CNT) of the kidney, where it functions as a highly selective epithelial calcium channel, playing a crucial role in Ca^{2+} reabsorption. While TRPV5 is predominantly found in the kidney, it is also expressed at lower levels in other tissues such as the brain and bone, where it has been shown to be essential for bone resorption by osteoclasts[5,6].

TRPV5 channels, similarly to most members of the TRPV subfamily, form a functional tetramer at the cell surface assembled by subunits containing six transmembrane domains with large intracellular N- and C-termini. The pore domain consists of the S5, loop, and S6 segments of each subunit, which assemble symmetrically in a four-fold structure to create a central ion conduction pathway[7,8]. The re-entrant pore loop of each subunit forms the extracellular part of the pore and functions as a selectivity filter, determining ion permeability, with a single aspartic residue at position 542 acting as a Ca^{2+} selectivity filter[9,10]. The S6 helices line the intracellular pore and form the gate at its narrowest part. TRPV5 inactivates in response to Ca^{2+} entry, a process mediated by calmodulin (CaM) binding to the channel[11] promoted by the interaction between the last residue at the end of the S6 gate of the channel, the highly conserved W583, with a C-terminal lysine of the CaM, which blocks the flow of ions through the pore[7,12]. The disruption of CaM binding leads to increased TRPV5 expression at the plasma membrane by avoiding channel retention in the endoplasmic reticulum[13]. The tryptophan residue W583 is highly conserved in TRPV5 across various species, but it is absent in other members of the TRPV family and is crucial for channel gating[14].

TRPV5 channels display marked inward rectification and are constitutively open at negative potentials, allowing for passive entry of cations into cells at the resting membrane potential. Regulation of TRPV5 is mainly carried out by the control of phosphatidylinositol 4,5-bisphosphate (PI(4,5)P2) lipid concentration, which binds between the

[1]Departamento de Fisiología, Facultad de Medicina, UNAM, Mexico City, Mexico. [2]Department of Systems Pharmacology and Translational Therapeutics, Perelman School of Medicine, University of Pennsylvania, Philadelphia, PA, USA. [3]Institute of Structural Biology, Perelman School of Medicine, University of Pennsylvania, Philadelphia, PA, USA. [4]Departamento de Neurociencia Cognitiva, Instituto de Fisiología Celular, UNAM, Mexico City, Mexico. [5]These authors contributed equally: Angélica Méndez-Reséndiz, José J. De Jesús-Pérez. ✉e-mail: vmb@pennmedicine.upenn.edu; leon.islas@gmail.com

N-linker, S4-S5 linker, and the S6 helix to keep the channel open[12]. Signaling by vitamin D, which mostly regulates expression of protein at the plasma membrane[15] and by parathyroid hormone, which acts through PKA phosphorylation[16], also regulates the channel. The long-chain lipid acyl-coenzyme A is a highly efficient activator of TRPV5 that binds to the same site as the endogenous ligand PI(4,5)P2 and induces very similar conformation changes to open the channel[17].

TRPV5 channels have a relatively limited pharmacology, with only a few known additional endogenous activators, such as PKC activator 1-oleoyl-acetyl-sn-glycerol and the β-glucuronidase, Klotho, that hydrolyzes extracellular sugar residues of TRPV5[18,19]. Conversely, TRPV5 is inhibited by synthetic compounds, including TH-1177[20], cannabinoids[21], and a higher specificity inhibitor, ZINC17988990[22].

Econazole and miconazole are antifungal agents that act as inhibitors of TRPV5. These compounds bind to a specific pocket situated between the S4 and S5 transmembrane domains[23], which is shared with TRPV6 channels[24] and likely act as allosteric inhibitors of channel opening. Additionally, ruthenium red is a non-selective inhibitor of many ion channels. In the case of TRPV5, it binds to the pore domain, likely blocking conduction and stabilizing the channel in a closed state[24,25].

Menthol is a highly membrane-permeable monoterpene alcohol derived from the mint plant (*Mentha sp.*) and a known activator of cold-sensing TRPM8 channels[26]. Menthol is an interesting compound that has been associated with renal toxicity and impaired intestinal mobility[27,28], which could be mediated in part by TRPV5 and TRPV6 ion channels. Menthol also activates or inhibits other TRP channels, such as TRPV3, TRPV1, and TRPA1, although the structural mechanisms involved are not known[29–32]. TRPV5 and TRPV6 are only 30% similar to other TRPVs, which suggests that different mechanisms of modulation by menthol.

Given its potential effects on renal and gut physiology and lack of mechanistic information, we explored menthol's actions on TRPV5 channels. Here, we show that it acts as a blocker of TRPV5. We show that menthol inhibits current through TRPV5 expressed in HEK293 cells by producing long-lived closures, likely corresponding to slow blocking events. We solve the structure of rabbit TRPV5 in complex with menthol by cryo-EM and find that a key determinant of menthol

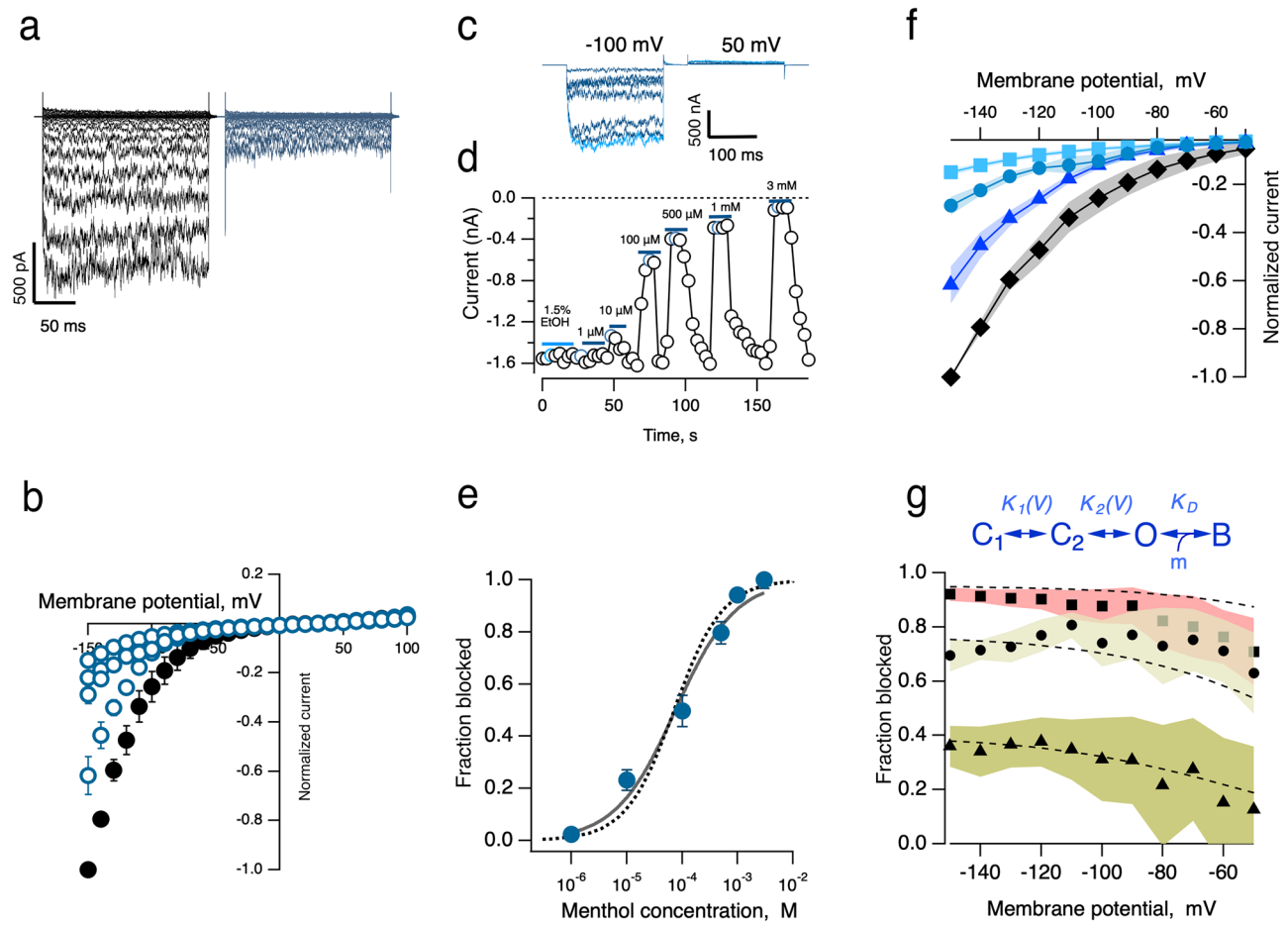

Fig. 1 | Menthol blocks rabbit TRPV5 channels. a Currents in response to voltage-clamp steps of 200 ms durations from −150 to 50 mV. Left panel in the absence and right panel in the presence of 500 µM menthol. **b** Current-voltage relationship of currents as in (**a**). Black circles, control; blue circles, menthol, $n = 6$ independent membrane patches. Data are shown as mean ± SEM. **c** Representative current traces of rbTRPV5 channels from an outside-out patch at −100 mV with increasing concentrations of menthol. Light blue trace was obtained by applying recording solution containing only 1.5% ethanol (vehicle) as a control. The rest of the traces are currents in the presence of increasing menthol concentration. **d** Time course of rbTRPV5-mediated current inhibition by menthol at increasing concentrations applied to the outside-out patch in (**c**). **e** Dose-response curve obtained from $n = 7$ outside-out patch recordings. The black curve is the fit to the Hill equation (Eq. 1) with the parameters $IC_{50} = 142.6\ \mu M \pm 18.3\ \mu M$ and Hill coefficient, $n_H = 0.75 \pm 0.064$. The dotted curve is the fit to the dose response predicted by Scheme I in (**g**) at −100 mV (Supplementary Note, Eqs. (4–7)). **f** Current-voltage relationships at 0 mM (diamonds), 3 mM (squares), 500 µM (circles) and 100 µM (triangles) menthol plotted in the interval -150 to −50 mV. Symbols are the mean of $n = 6$ independent outside-out patches. Shaded areas indicating the SEM. **g** The fraction of current blocked as a function of voltage at 3 mM (squares), 500 µM (circles) and 100 µM (triangles) menthol. Symbols are the mean of $n = 6$ independent outside-out patches. Shaded areas indicating the SEM. The dashed lines are the predicted blocked fractions at the indicated menthol concentration. The parameters of the model $K_1(0) = 0.2$; $K_2(0) = 0.22$, $q_1 = -0.1\ e_o$, $q_2 = -0.6\ e_o$, $K_D = 140\ \mu M$.

https://doi.org/10.1038/s41467-026-70759-8

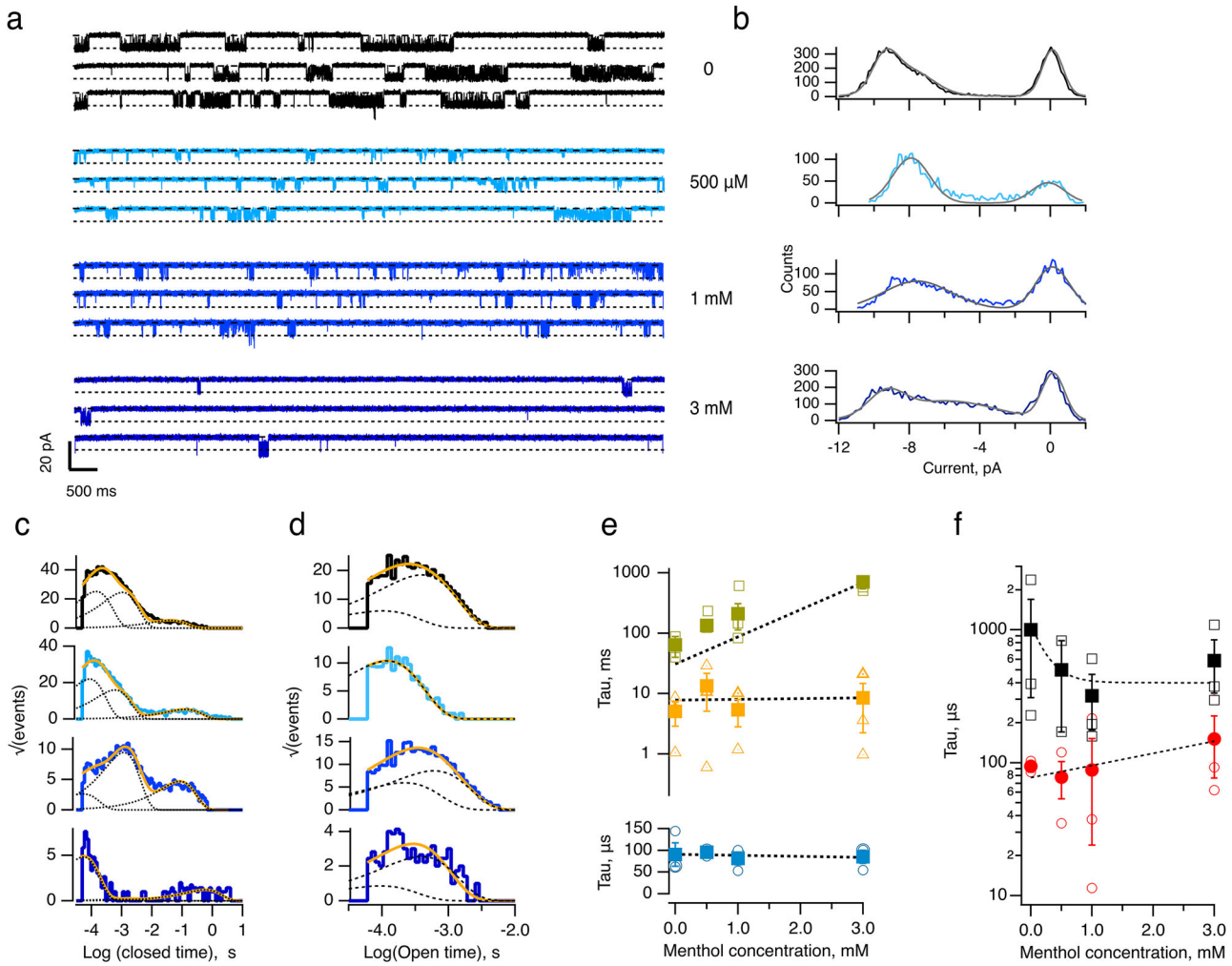

Fig. 2 | Single channel analysis reveals menthol is a slow blocker of rbTRPV5 channels. a Representative single-channel current traces of rbTRPV5 channels from an outside-out patch recorded at −100 mV in the presence of the indicated menthol concentration. The dashed and dotted lines indicate the closed and open amplitude, respectively. **b** All-points histograms of selected sections of records in (**a**), indicating the current amplitude of a single-channel opening. Histograms are fitted to the sums of three Gaussian functions. The main current amplitudes are as follows: no menthol, −9.46 ± 1.4 pA; 500 µM, −8.1 ± 1.47 pA; 1 mM, −7.66 ± 2.7 pA; 3 mM, -9.51 ± 0.99 pA. **c** Closed time distributions at increasing menthol concentrations. From top to bottom, no menthol, 500 µM, 1 mM and 3 mM menthol. Each histogram is fitted to the sum of three exponential components (orange), and each component is indicated by the dotted curves. **d** Open time histograms. Same order as in (**c**). Two exponential components are fitted to each histogram, indicated as in (**c**). **e** The dependance of the three closed time constants on the menthol concentration. Dotted lines are fits to linear equations and have no theoretical meaning. Blue, fast time constant, yellow, intermediate time constant, green, slow time constant (Table 1). Filled symbols are the mean value and error bars are ± SEM determined from $n = 3$ independent outside-out patches. **f** Dependance of the two open time constants on menthol concentration (Table 2). Filled symbols are the mean value and error bars are ± SEM determined from $n = 3$ independent outside-out patches. The slow open time constant data (black squares) is fitted to the empirical Eq. 3. The fast open time constant data (red circles) is fitted to a linear equation.

inhibition is a tryptophane residue at position 583 located at the intracellular entrance of the pore. Mutations W583Q and I575S readily reduce the effects of menthol, suggesting that they are important mediators of the menthol interaction. Our results expand the repertoire of inhibitors of TRPV5 channels and have implications to understand possible effects of menthol in renal physiology.

Results

Menthol inhibits TRPV5 via a slow blocker mechanism

First, we assessed the effect of menthol on the rabbit TRPV5 (rbTRPV5) by applying 500 µM menthol to the external face of the membrane in outside-out patch configuration. Menthol rapidly inhibited more than 50% of the current at all voltages without altering current kinetics (Fig. 1a). This inhibitory effect was largely reversible and occurred in a dose-dependent manner across all tested voltages (Fig. 1b–d). Fitting the dose-response curve with a Hill equation (Eq. (1), we determined a half-maximal inhibitory concentration (IC_{50}) of 142.6 µM and a Hill coefficient (n_H) of 0.75, suggesting that a single menthol molecule is sufficient to induce inhibition (Fig. 1e).

Interestingly, menthol block of TRPV5 is slightly voltage dependent, with the blocked fraction reduced at less negative potentials (Fig. 1f). Because menthol does not carry a net charge, we sought to explain this voltage-dependence by exploring the predictions of a multiple state model for block. We adapted a previously published three state gating model of TRPV5[14] and incorporated open state block (Scheme I, Fig. 1g). To constrain the model, we measured the voltage-dependence of single-channel channel openings, which indeed show that TRPV5 gating is intrinsically voltage dependent (Supplementary Fig. 1a, c). Scheme I explains the voltage dependence of menthol block because it is coupled to the open state and opening is itself voltage-dependent (Fig. 1g). This model also accounts for both the voltage and dose-dependence of block with the same set of parameters (Fig. 1e).

Table 1 | Closed time constants obtained by single-channel kinetic analysis of wild-type rbTRPV5 channels

Menthol concentration, (mM)	Slow time constant ± sem, (s)	Medium time constant ± sem, (s)	Fast time constant ± sem, (s)
0.0	64.05 ± 24.05	5.08 ± 2.19	$9.0 \times 10^{-5} \pm 2.6 \times 10^{-5}$
0.5	134.63 ± 9.03	13.36 ± 8.28	$9.5 \times 10^{-5} \pm 4.5 \times 10^{-6}$
1.0	209.93 ± 97.22	5.38 ± 2.58	$8.1 \times 10^{-5} \pm 1.4 \times 10^{-5}$
3.0	708.73 ± 166.89	8.49 ± 6.25	$8.5 \times 10^{-5} \pm 1.5 \times 10^{-5}$

Table 2 | Open time constants obtained by single-channel kinetic analysis of wild-type rbTRPV5 channels

Menthol concentration, (mM)	Slow time constant ± sem, (s)	Fast time constant ± sem, (s)
0.0	1000.23 ± 691.53	94.1 ± 8.9
0.5	500.4 ± 329.6	77.89 ± 24.39
1.0	319.63 ± 143.47	88.16 ± 64.16
3.0	586.66 ± 252.69	150.96 ± 74.12

Since the sequence of the inner pore region is highly conserved between mammalian TRPV5 and 6 channels, we examined the effect of menthol on the human TRPV5 orthologue and the related human TRPV6 channel, finding that both channels were also blocked by menthol with similar efficacy (Supplementary Fig. 2).

To further investigate the mechanism by which menthol inhibits TRPV5 currents, we analyzed single-channel recordings. Recordings from patches containing a single TRPV5 channel at −100 mV showed that gating was characterized by openings that occur in bursts (Fig. 2a). The single-channel current amplitude remained unaffected by menthol, as indicated by all-points amplitude histograms of selected current segments (Fig. 2b). In contrast, menthol increased both the frequency and duration of non-conducting events in a dose-dependent manner. To quantify this effect, we idealized channel openings and compiled open and closed dwell time histograms (Fig. 2c, d). The gating behavior of TRPV5 shows three exponential components in the closed-time distribution and two components in the open-time distribution (Tables 1 and 2). The number of exponential components in these distributions represents the minimum number of closed or open states. In this case, data indicates there are three closed or non-conductive states and one or two open states. These kinetics are consistent with the model in Scheme I (Fig. 1g), although this is not a definitive model.

Further analysis of single-channel recordings shows that menthol induces a concentration-dependent lengthening of the longer closed-state durations, while reducing the slow component of the open-state durations, consistent with menthol blocking ion conduction and shortening the length of bursts of openings (Fig. 2e, f and Tables 1 and 2). These findings indicate that menthol inhibition occurs via a blocking mechanism that does not alter single-channel current amplitude, a characteristic feature of slow channel blockers[33].

Structural mechanism of TRPV5 blockade by menthol

To gain structural insight into the molecular mechanism by which menthol blocks TRPV5, we determined the cryoEM structure of full-length rabbit TRPV5 in complex with menthol. A priori, it is unclear whether menthol solely blocks the channel or also induces an alternative conformational state to close the channel. Given that TRPV5 adopts an open state in the presence of $PI(4,5)P_2$, we initiated our experiments with a PIP_2-activated channel and subsequently applied menthol to assess its effect, which are similar conditions to those in which current recordings are performed. First, purified TRPV5 embedded in lipid nanodiscs was incubated with 400 μM $PI(4,5)P_2$ for 45 min to activate the channel, followed by the addition of 1 mM menthol and further incubation for 30 min before vitrification. CryoEM data processing yielded a structure at 3.37 Å resolution in a single conformational state, without imposed symmetry, which we refer to as $TRPV5_{PIP2+Menthol}$, (Supplementary Fig. 3 and Supplementary Table 3).

The $TRPV5_{PIP2+Menthol}$ structure reveals a clear density at the intracellular entrance of the pore, positioned between the S6 helices, consistent with presence of the menthol molecule (Fig. 3a, b). Importantly, this density was not observed in the previous published $TRPV5_{PIP2}$ structures[24,25] (Supplementary Fig. 4d). The model suggests that one molecule of menthol is primarily coordinated by two W583 residues, forming a potential hydrogen bond (2.8 Å) between its hydroxyl group and the amide group of W583, as well as a CH-π interaction (3.3 Å) with the indole ring of the adjacent W583 residue. Notably, W583 has been previously shown to coordinate the binding of a lysine residue from CaM, which also inhibits TRPV5[7,34], and to stabilize the ligand ciss-22a in TRPV6[35].

Comparing $TRPV5_{PIP2+Menthol}$ structure with the control structure, TRPV5 in the presence of $PI(4,5)P_2$ ($TRPV5_{PIP2}$)[17], we found that the pore remains in a semi-open state (RMSD = 0.5 Å) (Fig. 3c–i). Specially, the presence of menthol within the pore slightly reduces the pore diameter at I575. This effect is accompanied by a conformational change in the rotameric angle of W583, which shifts to accommodate hydrophobic interactions with the ligand. As a result, the pore at W583 adopts a conformation closely resembling the apo state (Fig. 3f). Consistent with this observation, we detected densities at the $PI(4,5)P_2$ binding site that resemble partially a $PI(4,5)P_2$ molecule (Supplementary Fig. 4e). These densities, as previously reported, are in contact with the basic residues R302, R305, K484, and R584, where the interaction with R584 being one of the most important for inducing the open conformational state[12,17,34]. Both our patch-clamp and cryo-EM results suggest that menthol blocks TRPV5 in the open state, a mechanism like that of CaM, further reinforcing the role of W583 as a key regulatory site for channel modulation.

Menthol binds to W583 in TRPV5 channels

To functionally validate this interaction, we introduced the W583Q mutation, which removes potential hydrophobic and aromatic interactions while preserving side-chain size and introducing a polar group. The W583Q mutation significantly reduced menthol-induced inhibition, shifting the dose-response curve to higher concentrations (IC_{50} = 3.7 mM, Fig. 4a, c), indicating that W583 is critical for menthol binding, as suggested by the cryo-EM structure. Single-channel recording confirmed the reduced inhibition by menthol of this mutant. W583Q channels exhibited distinct gating behavior compared to WT. Whereas WT TRPV5 opens in bursts, W583Q channels displayed continuous opening and closing events (Supplementary Fig. 5), similar to the previously reported W583L mutation[14]. The closed-time distribution contained two time-constants that remined unaffected by menthol, while the open-time distribution was fitted with two exponentials components (Supplementary Tables 1 and 2), consistent with Scheme I, indicating that the mutations did not greatly alter channel gating. W583Q showed a slight reduction in the slow component with increasing menthol concentrations. At the highest concentrations, in contrast to WT channels, menthol reduced the single-channel current amplitude in W583Q, suggesting that in

https://doi.org/10.1038/s41467-026-70759-8

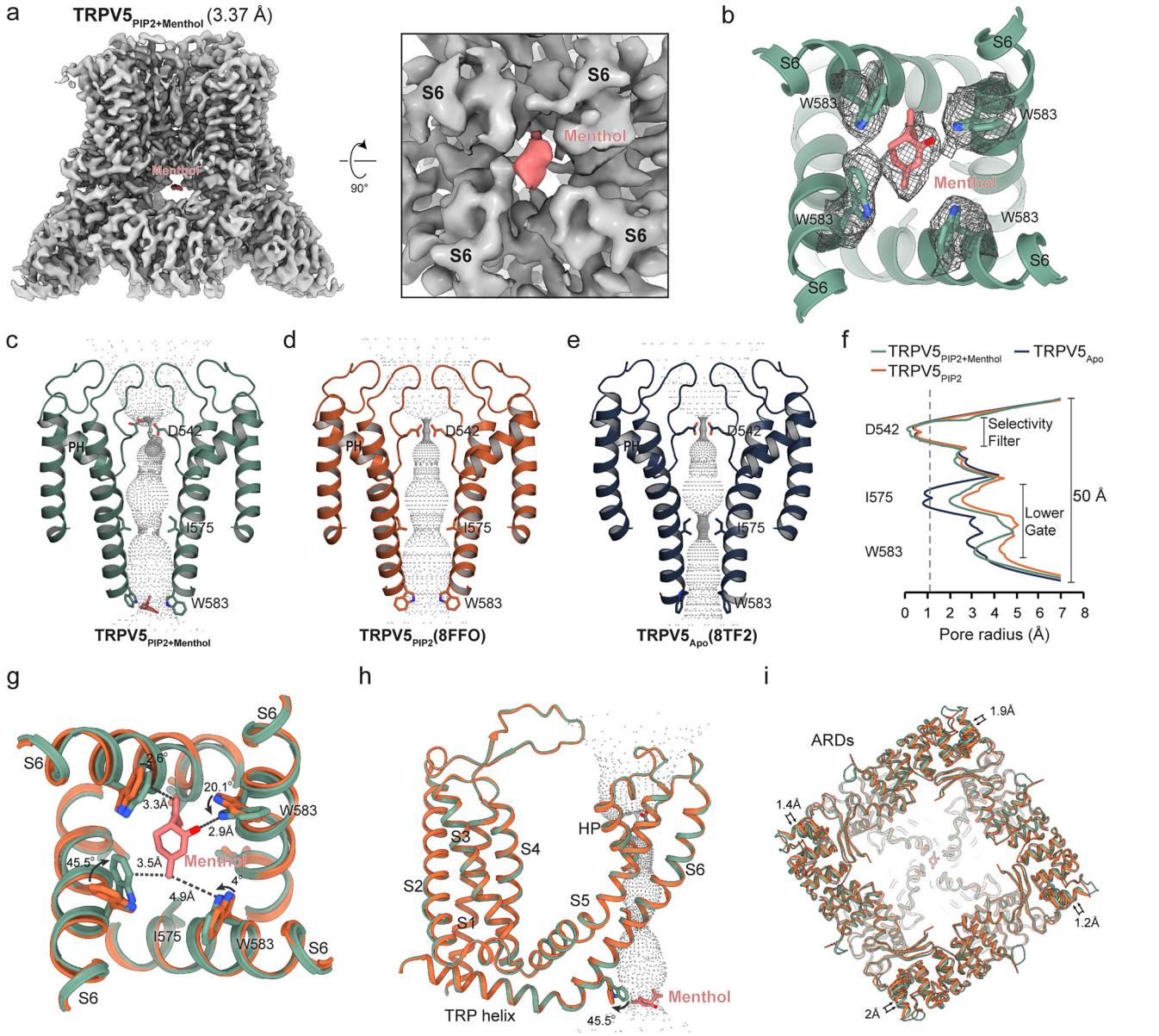

Fig. 3 | TRPV5 channel in complex with menthol in presence of PI(4,5)P_2. a The TRPV5-menthol density map (contoured at $\sigma = 4.0$) with no symmetry and a view from the intracellular site depicts the menthol binding site formed by S6 helices from each subunit, the menthol density is highlighted in coral. **b** The coordinate model of menthol binding site with overlaid density contoured at $\sigma = 3.0$. The map was contoured at 0.09 on chimeraX. W583 and menthol densities were selected using the coordinate model within the 3.5 Å range and split using *splitbyzone* chimera command. Pore profile of the TRPV5 in presence of PI(4,5)P_2 and menthol ($TRPV5_{PIP2+Menthol}$) **c** $TRPV5_{PIP2}$ **d** and $TRPV5_{Apo}$ **e**. **f** Pore radius along the conducting pathway of $TRPV5_{PIP2+Menthol}$ (green), $TRPV5_{PIP2}$ (orange), and $TRPV5_{Apo}$ (blue). The dotted gray line at 1.1 Å represents the dehydrated calcium radius. **g** Coordinate model comparison of internal gate, membrane helices (S1-S6) **h** and ARDs domains **i** between $TRPV5_{PIP2}$ (orange) and $TRPV5_{PIP2+Menthol}$ (green). Structural rotation and displacements are indicated by curved and straight arrows, respectively. Distances between the menthol and the residue W583 are shown in dash gray lines.

the absence of a tryptophane at position 583, menthol behaves as a fast blocker, accounting for the remaining block (Supplementary Fig. 5d).

Despite this mutation producing a gain-of-function phenotype, shifting channel open probability and the I-V curve to more positive potentials (Supplementary Fig. 1b,c and Supplementary Fig. 6b,c, respectively), W583Q retained the inward rectification characteristic of TRPV5 (Fig. 4a and Supplementary Fig. 6a). Furthermore, the mutant was also blocked by the pore blocker ruthenium red (RR) with an IC_{50} close to that of WT channels, indicating that the mutation does not alter the pore architecture and that its effect is specific to block by menthol (Supplementary Fig. 7).

Menthol block was also tested in the previously characterized W583A mutant, for which a cryo EM structure exists[7] (Fig. 4b). Similarly to W583Q, W583A showed reduced menthol block (Fig. 4b, c). The observation that both small or large polar substitutions at position W583 greatly impair menthol binding, supports the importance of hydrophobic interactions in stabilizing menthol binding.

Our cryo-EM structure further suggests that menthol may be stabilized at its binding site through a hydrogen bond between its hydroxyl group and the indole of W583 (Fig. 4d). To test this interaction, we substituted W583 by a phenylalanine, which lacks an indole group and cannot form hydrogen bonds. The W583F mutant exhibited a right-shifted menthol dose-response curve, suggesting

https://doi.org/10.1038/s41467-026-70759-8

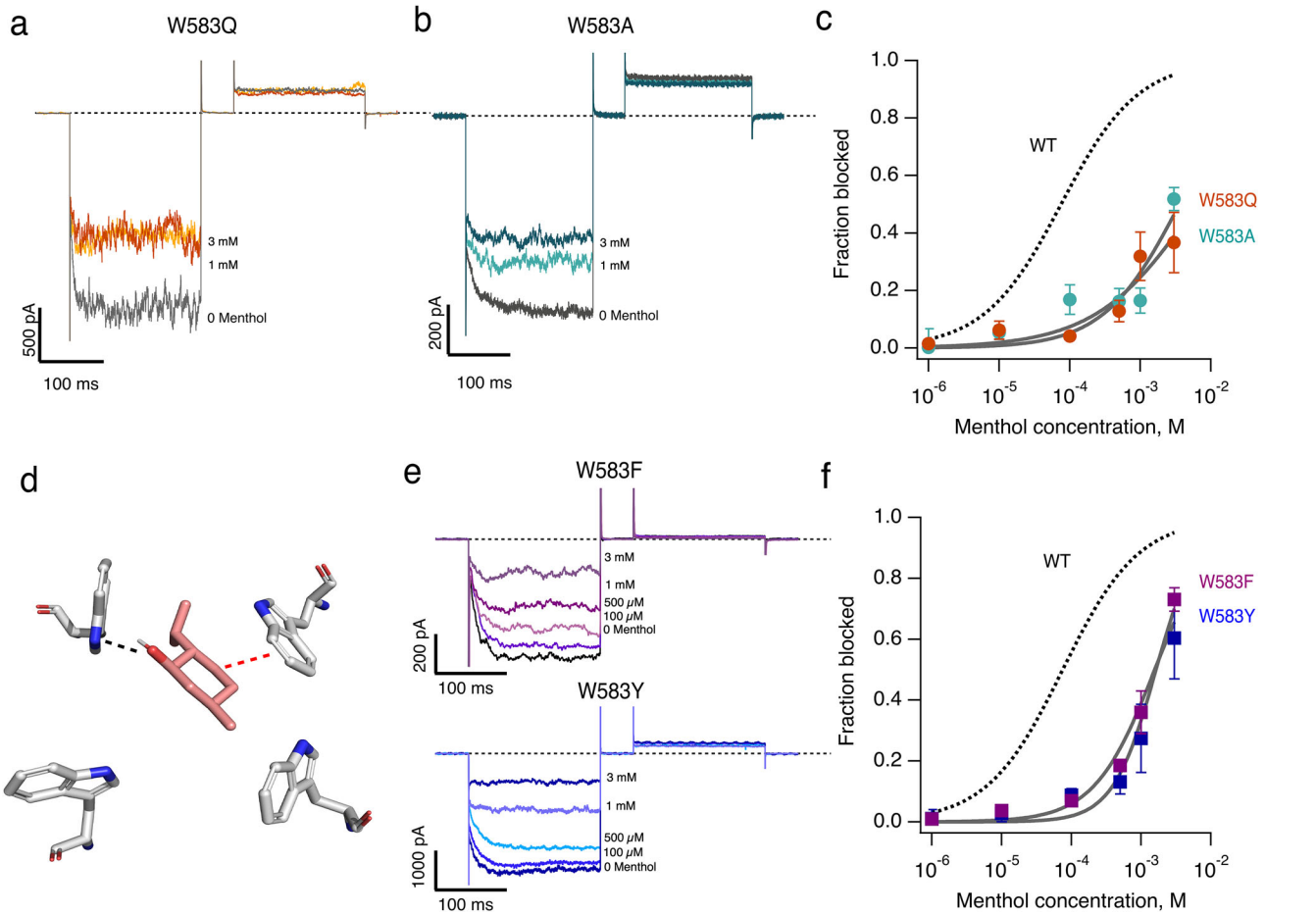

Fig. 4 | Effects of W583 mutations on menthol block of TRPV5. Representative macroscopic currents from rbTRPV5 mutants W583Q (**a**) and W583A (**b**) recorded from HEK293 cells in whole-cell configuration at −100 mV in the absence (gray) or presence of the indicated menthol concentrations. **c** Dose–response curves for menthol inhibition of W583Q (orange circles) and W583A (green circles) compared to WT TRPV5 (dashed line). Data are presented as mean ± SEM, with solid lines corresponding to Hill equation fits. For W583Q, IC_{50} = 3.70 ± 1.08 mM, n_H = 0.51 ± 0.085, n = 7. For W583A, IC_{50} = 3.6 ± 0.16 mM, n_H = 0.8 ± 0.29, n = 6. n represents the number of independent whole-cell recordings. **d** Structural model of the menthol binding site showing W583 side chains and ligand interactions, obtained by docking, including a potential hydrogen bond with the menthol hydroxyl group (black dashed line) and a CH–π contact with the indole ring of an adjacent W583 (red dashed line), suggesting a possible conformational position of menthol. **e** Representative whole-cell current traces from mutants W583F and W583Y at −100 mV in the absence or presence of increasing menthol concentrations. **f** Dose–response curves for menthol inhibition of W583F and W583Y compared to WT (dashed line). Data are presented as mean ± SEM, with solid lines representing Hill equation fits. For W583Y, IC_{50} 2.1767 mM ± 0.214 mM, n_H = 1.1944 ± 0.15, n = 7. For W583F, IC_{50} = 1.48 ± 0.09 mM, n_H = 1.33 ± 0.12, n = 7. n represents the number of independent whole-cell recordings.

reduced affinity (Fig. 4e, f). Similarly, W583Y, which retains hydrophobicity but introduces a hydroxyl group, also impaired menthol block. These results highlight the requirement for specific indole chemistry of tryptophane at position W583 for menthol coordination (Fig. 4e, f).

Since many W583 mutation produce gain of function phenotypes (ref. 14 and Supplementary Fig. 6), as control we introduced mutations at nearby positions. Mutations M578L and G579A, which are localized in the inner gate and near W583, yielded inwardly rectifying channels with menthol sensitivity similar to WT, confirming that the effects W583 substitutions on menthol block are specific and not due to gross alteration of pore structure (Supplementary Fig. 8). Importantly, G579A has previously been reported to yield stable macroscopic currents under divalent-free recording conditions[14]. In the same study, M578 was not identified as a major contributor to pore constriction, consistent with our observation that the M578L mutation does not affect menthol sensitivity (Supplementary Fig. 8).

As presented in the previous section, our structural and functional data reveal that menthol binds to the intracellular entrance of the TRPV5 pore, specifically interacting with residue W583 while the pore remains open. To probe the dynamics of menthol pore occupancy, we ran 500 ns all-atom molecular dynamics (MD) simulations of the open-state $TRPV5_{PIP2}$ structure (PDB: 8FFO), with menthol molecules initially placed randomly in the aqueous phase. Our results showed that the protein stabilized after ~20 ns (RMSD = 2–4 Å, Supplementary Fig. 9e), with minor fluctuations (RMSF ~ 2 Å) observed at the intracellular entrance of the pore (Supplementary Fig. 9f), suggesting that the presence of menthol does not induce substantial conformational changes in the protein. All four simulation replicas showed menthol entering and occupying the pore from intracellular site (Supplementary Fig. 9a, b). Trajectory analysis revealed that menthol molecules can permeate the plasma membrane (Supplementary Fig. 9d). No Na^+ permeation events occurred during any menthol-occupied state. To quantify the position of menthol relative to the pore, we measured its distance from I575 (Supplementary Fig. 9a, b). Unexpectedly, menthol remained at W583 for only a brief period, forming transient hydrogen bonds lasting 0.1–0.5 ns, before establishing an interaction with other residues inside the pore, particularly I575, which appeared to stabilize menthol. Once a menthol occupied the pore, additional menthol molecules interacted more frequently with W583 (Supplementary

https://doi.org/10.1038/s41467-026-70759-8

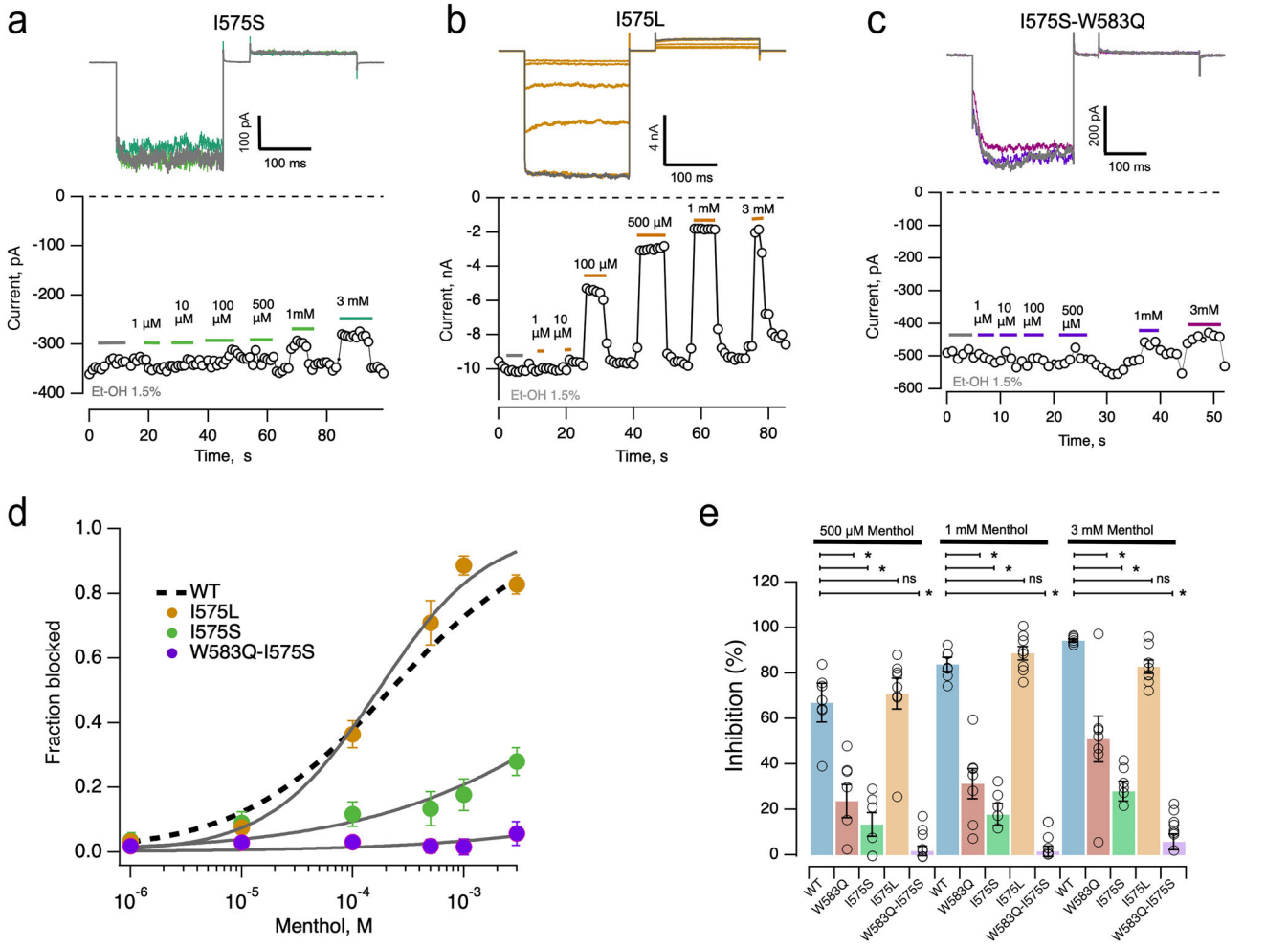

Fig. 5 | Effects of I575 mutations on menthol block of TRPV5. Representative macroscopic currents from rbTRPV5 mutants I575S (**a**), I575L (**b**), and the double mutant W583Q–I575S (**c**), recorded at −100 mV. Upper panels show current traces in the absence (gray) or presence of menthol (color traces). Lower panels show the time course of rbTRPV5-mediated current inhibition by menthol at increasing concentrations applied in whole-cell configuration from HEK293 cells. **d** Dose–response curves for menthol inhibition of I575S, I575L, and W583Q–I575S, compared with WT TRPV5 (black dashed line; IC_{50} = 142.6 ± 18.3 µM, nH = 0.75 ± 0.064). Solid lines represent Hill equation fits. For I575S: IC_{50} = 26.8 ± 9.3 mM, nH = 0.405 ± 0.0415; n = 7 independent whole-cell recordings. For W583Q–I575S the Hill equations can not be fitted with confidence; n = 12 independent whole-cell recordings. For I575L: IC_{50} = 121.3 ± 24.5 µM, nH = 1.44 ± 0.481; n = 9 independent whole-cell recordings. Symbols are the mean and error bars the SEM. **e** Percent inhibition at 500 µM, 1 mM, and 3 mM menthol for WT and mutant channels. Bars represent mean ± SEM, with individual data points overlaid. Statistical comparisons were performed using unpaired, two-tailed Student's t-tests, with each mutant compared to WT at the corresponding menthol concentration. * Indicates statistical significance ($p < 0.001$); ns not significant. 500 µM: W583Q, $p = 5.9 \times 10^{-4}$; I575S, $p = 0.0000207$; I575L, $p = 0.585$; W583Q–I575S, $p = 4.30 \times 10^{-6}$. 1 mM: W583Q, $p = 9.62 \times 10^{-5}$; I575S, $p = 4.73 \times 10^{-6}$; W583Q–I575S, $p = 8.53 \times 10^{-14}$. 3 mM: W583Q, $p = 0.00512$; I575S, $p = 1.58 \times 10^{-5}$; I575L, $p = 5.32 \times 10^{-4}$; W583Q–I575S, $p = 1.68 \times 10^{-11}$. Values were determined from n independent whole-cell recordings (WT, n = 7; I575S, n = 6; I575L, n = 8; W583Q–I575S, n = 12; W583Q, n = 7).

Fig. 9c), suggesting that both W583 and I575 are key residues involved in menthol-mediated TRPV5 blockade.

Effect of mutations at position I575

To investigate the role of I575 in menthol binding, as suggested by the MD simulations, we tested the I575S mutant, which should eliminate hydrophobic interactions and introduce a polar residue. This mutation also diminished menthol inhibition, shifting the dose-response curve to higher concentrations and decreasing the fraction of blocked current, even at high menthol concentrations (Fig. 5a, d, e). The magnitude of this effect was comparable to that observed in W583Q, suggesting that menthol interacts with I575, or alternatively, that the presence of a polar residue at position 575 disrupts menthol interactions with W583. As a control, we tested the I575L mutation, which preserves a hydrophobic residue but could alter sidechain packing near the protein backbone and should induce little deformation. This mutant retains the menthol blocking affinity of WT (Fig. 5b, d, e). The results indicate that menthol might move from its W583 binding site to a deeper position within the pore and requires a hydrophobic amino acid at position 575.

Finally, we examined the W583Q-I575S double mutant. These channels remained inwardly rectifying and retained their affinity for the pore blocker ruthenium red (Supplementary Fig. 7), indicating that the combined mutations did not drastically alter TRPV5 gating. However, the double mutant exhibited significantly reduced susceptibility to menthol inhibition (Fig. 5c, d, e), almost completely eliminating block by menthol, confirming that both W583 and I575 are essential for menthol binding and TRPV5 blockade.

Discussion

TRPV5 channels play important physiological and pathophysiological roles. As key regulators of calcium homeostasis, mutations in human TRPV5 and knockout models in mice have implicated this channel in nephrolithiasis[36], progression and prognosis of certain cancers[37,38], and

bone resorption[5]. Given the expanding significance of TRPV5, understanding its regulatory mechanisms and interactions with pharmacological agents is of considerable interest.

Menthol is a hydrophobic molecule that can partition and cross phospholipid membranes at low concentrations and readily partition into cells[39]. Menthol's capacity to penetrate cell membranes is often exploited to increase the cell penetration of other organic compounds[40]. This property makes menthol a molecule of physiological interest.

In this study, we demonstrated that menthol, a monoterpene, blocks cation conduction through TRPV5 channels. Our experiments indicate that menthol acts as a slow open-channel blocker, consistent with our cryoEM structure of the TRPV5-menthol complex. This structure reveals that menthol binds at the intracellular entrance of the pore, interacting with the aromatic residue W583, which adopt orientations that facilitate close interactions with the ligand. Additionally, the structure shows that menthol induces a conformational change in the inner pore, reducing its diameter and likely representing a closed state.

Mutagenesis experiments confirm the functional importance of W583 for menthol binding and further show that specific interactions, including hydrogen bonding and hydrophobic interactions with the indole group of W583 are needed for menthol coordination.

Although our structural data indicate a stable W583-mediated menthol-binding site, the MD trajectories reveal additional transient interactions that show that menthol is more dynamic near the pore. Two factors likely account for this behavior: the force field used (CGenFF) and the simulation temperature (29.8 °C). For example, in our system the calculated dipole moment of menthol in solution is ~2.1 D, slightly higher than the previously reported value of 1.4 D[41]. Likewise, the estimated menthol diffusivity at 4 °C is ~3.7×10^{-10} m^2/s versus ~8×10^{-10} m^2/s at 29.8 °C. As a result, over a 100-ns trajectory menthol would, on average, sample ~4.7 nm at 4 °C and ~7 nm at 29.8 °C, increasing the probability of exploring alternative poses in silico. Moreover, our simulations (~500 ns) are short relative to the timescales required for experimental equilibration, so we cannot rule out that menthol would converge onto the single W583-mediated pose at longer timescales or under different sampling strategies. Despite these caveats, the MD results were essential for guiding mutagenesis, and this was validated experimentally: the I575S and W583Q-I575S mutations drastically reduced the potency of menthol blocking, indicating that menthol dynamically interacts with these two residues.

Single-channel analysis provides mechanistic insights into menthol inhibition, supporting its role as a slow channel blocker binding to W583. This interpretation is reinforced by the marked increase in the number and duration of shut dwell times with menthol concentration. When W583 is substituted with a glutamine (W583Q), menthol shifts its primary interaction to I575. However, this interaction is much more transient, leading to rapid block and reduced single-channel current. The shifting of menthol from W583 to a deeper position near I575 is reminiscent of the mechanism of block by quaternary ammoniums in potassium channels. For instance, tetra-butyl ammonium (TBA) binds to phenylalanine in the inner pore of hERG channels and then moves further up the pore to interact with a narrow region formed by an isoleucine[42].

The importance of W583 in TRPV5 and TRPV6 has previously been established in controlling calcium permeation and mediating interactions with calmodulin[7,12]. Recently, a novel class of TRPV6 inhibitors, (4-phenylcyclohexyl) piperazine derivatives (PCHPDs), was identified[35]. These compounds bind to a region equivalent to the menthol-binding site in TRPV5, suggesting a conserved druggable pocket for TRPV5/TRPV6 channel blockers.

Interestingly, in our structures, TRPV5 bound to PIP_2 and menthol preserves an overall C4 symmetry, yet this arrangement is locally perturbed at the ligand-binding site. This contrasts with TRPV5 in complex with calmodulin or TRPV6 bound to cis-22, where C4 symmetry is maintained even at the W583 binding site. We interpret this localized disruption as a consequence of menthol's pronounced molecular asymmetry. One terminus of menthol contains a donor/acceptor region capable of forming strong hydrogen-bonding interactions with the NH group of W584, while the remainder of the molecule is densely populated with CH groups, favoring CH−π interactions with tryptophan aromatic rings. The small molecular size of menthol likely prevents simultaneous engagement with all four W583 residues, limiting its capacity to induce the large-scale conformational rearrangements of the pore observed in other TRP family members, such as TRPV2 and TRPM2, which transition to a global C2 symmetry upon activation by RTX or during intermediate gating steps, respectively[43,44]. Instead, the conformation captured here appears to represent a hybrid between the canonical PIP_2-bound open state and a partially obstructed state in which two adjacent W583 residues are stabilized by menthol in a geometry optimal for impeding ion conduction.

The menthol binding site in TRPM8 differs significantly from the site identified in TRPV5, despite the similarity between the IC_{50} for TRPM8 activation (62.6 μM)[45] and the IC_{50} for TRPV5 inhibition (142.6 μM). In TRPM8, menthol interacts with R842, Y745, and Y1005, located within the S1-S4 transmembrane domain[46]. Menthol also activates TRPV3, potentially via interactions in the S4-S5 linker domain with glycine and arginine residues, leading to partial activation[30]. It has been proposed as an antagonist of mammalian TRPA1 and activator of TRPV1[29], although it is also reported as an inhibitor of TRPV1[31], though the precise mechanisms remain unclear. Recent reports indicate that menthol inhibits TRPV4 function, decreasing GSK-induced cytosolic Ca^{2+} in mouse sweat glands[32].

Menthol exhibits striking species-dependent effects on TRPA1. While non-mammalian TRPA1 channels are insensitive to menthol, mammalian TRPA1 channels display dual responses: low concentrations (~50–70 μM) activate the channel, whereas high concentrations (250 μM) inhibit it. In human TRPA1, menthol acts exclusively as an activator[29,47,48]. Beyond TRP channels, menthol interacts with a variety of membrane proteins, including voltage-gated calcium and sodium channels and several neurotransmitter receptors[49,50].

The menthol inhibition mechanism described here might be unique to TRPV5 and TRPV6 channels, due to the fact that these channels show only 30% sequence identity to the rest of the TRPV subfamily[51] and are the only ones with a critical tryptophane at position 583 in the lower pore. As discussed above, menthol exhibits diverse actions across TRP channels, our study shows that in TRPV5, menthol engages a distinct mechanism by interacting with W583 at the lower gate to function as a slow pore blocker, thereby broadening our understanding of how menthol differentially modulates TRP channel function beyond the mechanism elucidated for activation of TRPM8.

While it is widely recognized as a TRPM8 activator[46], several studies have raised concerns about its impact on renal physiology. Menthol has been reported to cause proximal tubular cell toxicity[28]; toxicological reports describe renal dysfunction and acute kidney failure following high-dose exposure (approximately 24 mM in the diet)[52]. Although these findings point to potential renal consequences, the underlying mechanisms remain unclear, and information on the role of menthol in kidney physiology is still limited. Thus, the kidney represents an important and underexplored field for investigating the actions of menthol, particularly in relation to the physiological and pathophysiological role of TRPV5.

On the other hand, the impact of TRPV5 inhibition may differ substantially in non-renal contexts, particularly in cancer. Dysregulation of TRPV5 and 6 channels has been associated with disrupted Ca^{2+} homeostasis, increased migration, and altered growth signaling in renal cell carcinoma and other malignancies[37,53]. These observations

suggest that inhibition of these channels may be of potential therapeutic use in cancer biology.

Methods

Molecular biology and cell transfection

The gene encoding full-length rabbit TRPV5 (rbTRPV5; UNIPROT id: Q9XSM3·TRPV5_RABIT) ion channel cloned in pCINeo/IRES-GFP was a gift from Dr. Tibor Rohacs (Rutgers University). This is a bicistronic plasmid containing both the channel and a GFP (UNIPROT id: Q17105_AEQVI) sequence under separate promotors, allowing identification of transfected cells by looking for GFP-fluorescent cells. Human TRPV5 (UNIPROT id: Q9NQA5·TRPV5_HUMAN) was subcloned in the pCDNA3.1(+) vector and was a gift from Dr. Sharona Gordon (University of Washington). TRPV6 (UNIPROT id: Q9H1D0·_HUMAN) was cloned from human placenta and was donated to us by Dr. Tibor Rohacs[54]. Residue numbers refer to the human TRPV5 sequence (729 amino acids); the corresponding regions in human TRPV6 (725 aa) and rabbit TRPV5 (730 aa) are conserved, so numbering is the same across all three proteins in this study.

Single and double mutations were introduced into the rbTRPV5 gene using mutagenic oligonucleotides in whole-plasmid PCR reactions employing KOD Hot Start DNA polymerase (Novagen-Millipore Corp.) according to the manufacturer's instructions. PCR products were treated with 1 µl DpnI restriction enzyme (New England Biolabs) and incubated 5 h at 37 °C to remove the parent plasmid. The samples were transformed into DH5α *E. coli* competent cells. For each mutant, five colonies were picked and inoculated in 5 mL LB medium, and the plasmids were extracted using a home-made miniprep procedure[55]. Mutants were confirmed by automatic sequencing.

Plasmids encoding hTRPV5, hTRPV6, and rbTRPV5-IRES-GFP wild-type and with mutations were transfected into Human Embryonic Kidney 293 (HEK293) cells (ATCC CRL-1573) using the JetPei reagent (Polyplus Transfection, France) according to the provider's protocol. Cells were maintained in Dulbecco's modified Eagle's medium (DMEM) (Gibco, Grand Island, NY, USA) supplemented with 10% fetal bovine serum and 1% of antibiotics (penicillin and streptomycin) (Invitrogen USA), at 37 °C, in a 5% CO_2 atmosphere and were reseeded every 3 days using 0.05% trypsin-ethylenediaminetetraacetic acid (Trypsin-EDTA) in 35 mm culture dishes over glass coverslips for subsequent electrophysiology assays. Experiments were performed 19–24 h after transfection with 1 µg of rbTRPV5-IRES-GFP (wild-type or mutant). Due to the low cell viability observed after expression of most mutants, a separate plasmid encoding pEGFP-N1 was introduced to enhance the identification of transfected cells. For single-channel recordings, 25 ng of wild-type or mutant DNA for 24 h was used, along with 100 ng of the pEGFP-N1 plasmid, to identify transfected cells.

Patch-clamp recording and data analysis

For patch-clamp recordings, transfected cells were identified as green-fluorescing cells using an inverted microscope (Nikon Ti) with LED-based fluorescence illumination (478 nm excitation, 505 nm dichroic mirror, 535/40× nm emission filter) and a 40× objective. Macroscopic currents from HEK293 cells expressing wild-type or mutant channels were obtained in the outside-out configuration, employing the following divalent-free extracellular (pipette) and intracellular (bath) solutions (in mM): 140 NaCl, 10 EGTA (ethylene glycol-bis(β aminoethyl ether)-N,N,N′,N′-tetraacetic acid), 10 HEPES (4-(2-hydroxyethyl)−1 piperazineethanesulfonic acid); intracellular (bath); 140 NaCl, 10 EGTA, 10 HEPES, adjusted to pH 7.2 with NaOH. Menthol or recording solution was applied by placing the outside-out patch in front of a gravity-feed perfusion system. All chemicals for solutions were acquired from Sigma-Aldrich. Recording pipettes were pulled from borosilicate capillary glass (Sutter Instruments) using a P-97 puller (Sutter Instruments) and fire polished to a final resistance in recording solutions of 3–5 MΩ. Currents were elicited by voltage-clamp pulses from −100 to 50 mV of 200 ms duration applied every 3 s and monitored for several minutes during menthol application. Current-voltage (I-V) curves were obtained by changing the membrane potential in 10 mV steps from −150 to +100 mV (200 ms duration) every 3 s at a 0 mV holding potential.

Currents were normalized to the initial current at −150 mV to obtain I/I_{max} and then averaged. To obtain dose-response curves, currents recorded at −100 mV at each concentration of (-)-menthol were normalized to the initial current obtained without the compound and in the presence of 1.5% ethanol. Dose responses are plotted as the fraction of blocked current vs. menthol concentration, *[menthol]* and the dose-response curves were fitted to Hill equation:

$$\frac{I}{I_{\max}} = \left(\frac{1}{1+\frac{[menthol]}{IC_{50}}}\right)^{n_H} \quad (1)$$

where IC_{50} is the half-inhibitory concentration and n_H is the Hill coefficient.

Single-channel currents were also recorded from outside-out patches with pipettes having 7–8 MΩ resistance. Continuous recordings of at least 1 min duration at −100 mV were obtained before and after the application of menthol to the outside of the patch. Three menthol concentrations were applied to the same patch separated by washing in recording solution. Data were filtered at 3 kHz and sampled at 50 kHz with an EPC 10 patch-clamp amplifier (HEKA Elektronik) run by Patchmaster software (HEKA Elektronik). Open and closed dwell times were detected employing the 50% threshold crossing technique[56]. Dwell time histograms were compiled and plotted using the logarithmic transform of[57] and fitted to sums of equally transformed exponential functions using a least-squares method to determine time constants associated with opening, closing and blocking events. Events shorter than the filter dead time, d_t of 63 µs at 3 kHz, were excluded from the histogram and not considered for fitting. Single-channel analysis was performed with custom-written software. The voltage-dependance of the single-channel open probability $P_o(V)$, was fit to the following Boltzmann function:

$$P_o(V) = \frac{1}{1+e^{q(V-V_{0.5})/K_BT}} \quad (2)$$

Here, q is the apparent gating charge in elementary units, V is the applied potential, $V_{0.5}$ the voltage of half-maximal P_o and K_B is Boltzmann constant and T the temperature in Kelvin (room temperature 23 °C).

The open and slow mean open time constant data was fitted to the empirical equation:

$$\tau[menthol] = 545 - 380 * (e^{(-\frac{[menthol]}{0.009\,mM})}) \quad (3)$$

Due to reduced expression levels of several mutant channels macroscopic currents were recorded in the whole-cell configuration. On the day of recording, cells were briefly detached using Trypsin-EDTA and reseeded onto glass coverslips so they did not attach strongly to the glass surface. After obtaining the whole-cell configuration, cells were lifted and placed in front of the perfusion system for the application of different concentrations of menthol or ruthenium red. Single-channel currents from mutant channels were recorded using the same procedures for WT channels.

Preparation of menthol and ruthenium red solutions

(-)-Menthol was obtained from Santa Cruz Biotechnology, dissolved in absolute ethanol to form a stock solution at 200 mM, and then diluted

from this stock in recording solution at the desired concentration (1 µM, 10 µM, 100 µM, 500 µM, 1 mM, 3 mM). These working solutions were then sonicated for 5–10 min before use and prepared fresh for every recording day. The higher concentration of (-)-menthol used (3 mM) had a final ethanol concentration of 1.5% thus, 1.5% ethanol in recording solution was used as a control in all experiments after (-)-menthol application and it was determined that it did not affect channel currents.

Ruthenium red (Ammoniated Ruthenium Oxychloride, Sigma-Aldrich) was prepared as a stock solution at 100 µM in water. Dilutions were prepared from this stock to reach concentrations of 0.5 nM, 1 nM, 10 nM, 100 nM, 500 nM, 1 µM.

Igor Pro 8 software (Wavemetrics) was used for analysis, including fitting, single-channel analyses, statistical analysis, and figure preparation. Data were assumed to follow a normal distribution, and hypothesis testing was performed using unpaired, two-tailed Student's *t* tests.

TRPV5 protein preparation

TRPV5 preparation and purification followed the protocol described in ref. 34. Briefly, the rabbit TRPV5 with a C-terminal 1D4 epitope tag in a YepM vector[23] was transfected into BJ5457 *Saccharomyces cerevisiae* (ATCC) using an alkali-cation yeast transformation kit (MP Biomedicals), according to the instructions of the manufacturer. Transformed cells were plated on SD-Leu agar plates and allowed to grow at 30 °C for 2 days. 30-50 colonies were picked from a plate and inoculated into a single 125 mL starter culture containing SD-Leu media and 10% *v*/v glycerol. The culture was incubated at 30 °C until reaching the top of the log phase (OD 1.0–1.4). After confirmation of protein expression by Western blot, the cells were grown at 30 °C with shaking at 200 rpm in 2.5 L of media per flask until OD of 1.0–1.4 was reached. Cells were harvested by centrifugation at 3000 × *g*, resuspended in storage buffer (25 mM Tris-HCl, pH 8.0, 300 mM sucrose, and 1 mM PMSF) on ice, and then spun down at 3000 × *g* to discard the supernatant. Cell pellets were subsequently stored at −80 °C. This expression culture was propagated using 15 mL of the previous growth at OD 1.0–1.4 for several days until the desired amount was obtained.

Approximately 60 L of growth cells were thawed and resuspended in 300 mL of homogenization buffer (25 mM Tris-HCl, pH 8.0, 300 mM sucrose, 5 mM EDTA, and protease inhibitor cocktail). The resuspended cells were lysed using a M110Y microfluidizer (Microfluidics) at 100–120 psi. The membranes were separated from cellular debris by centrifugation at 3000 × *g* for 10 min, followed by centrifugation of the supernatant at 14,000 × *g* for 35 min. The membranes obtained from the previous spin were then pelleted at 100,000 × *g* for 1 h. The pelleted membranes were harvested and resuspended on ice using a 15 mL tissue homogenizer (Kontes Duall with PTFE pestle) in buffer containing 25 mM Tris-HCl, pH 8.0, 300 mM sucrose, and 1 mM PMSF, and stored at −80 °C.

TRPV5 was solubilized from the thawed membranes in solubilization buffer (20 mM HEPES, pH 8.0, 150 mM NaCl, 2 mM TCEP, and 0.87 mM LMNG). The insoluble fraction was separated by centrifugation at 100,000 × *g* for 1 h. The resulting supernatant was incubated with 1D4-antibody coupled to CnBr-activated Sepharose beads for 3 h. The beads were collected on a gravity flow column, washed with wash buffer (20 mM HEPES, pH 8.0, 150 mM NaCl, 2 mM TCEP, and 0.064 mM DMNG). The beads were incubated with elution buffer (20 mM HEPES, pH 8.0, 150 mM NaCl, 2 mM TCEP, and 0.064 mM DMNG, 3 mg/mL 1D4 peptide) overnight. TRPV5 was eluted in 1 mL fractions every 5 min. Peak fractions were pooled and concentrated using a 100-kDa concentrator (Millipore). For reconstitution into nanodiscs, an equimolar amount of MSP2N2 protein was incubated with the detergent-solubilized TRPV5 in the presence of soy polar lipids and DMNG detergent in a 1 mL reaction volume. The molar ratio of TRPV5:MSP2N2:lipid:DMNG in mixture was 1:1:200:500. Lipids and DMNG were dissolved in 20 mM HEPES, pH 8.0, 150 mM NaCl, 2 mM TCEP (SEC buffer). The reaction mixture was incubated on ice for 30 min, followed by the addition of ~30 µL of Bio-Beads. The mixture was rotated at 4 °C for 1 h. The supernatant was transferred to a new tube, and another 30 µL of fresh Bio-Beads was added before rotating at 4 °C overnight to complete the reaction. Reconstituted TRPV5 was subjected to a Superose 6 increase 10/300 GL column (GE Healthcare) equilibrated with SEC buffer. Fractions containing nanodisc reconstituted TRPV5 were pooled and concentrated to 2.57 mg/ml.

Cryo-EM sample preparation and data collection

$TRPV5_{PIP2+Menthol}$ sample was incubated with 400 µM diC8-PI(4,5)P_2 (Echelon Biosciences, Cat# P-4508) for 45 min and 1 mM Menthol (Sigma-Aldrich, Cat# 2216-51-5) for 30 min, corresponding to a 1:53:132 (TRPV5:PIP2:Menthol) molar ratio. Menthol was solubilized in 100% ethanol (200 mM) and then diluted at 15% in SEC buffer (30 mM). Final sample contained 1% ethanol. Three microliters $TRPV5_{PIP2+Menthol}$ sample were applied to glow-discharged 1.2/1.3 Quantifoil Holey Carbon Grids (Quantifoil Micro Tools) using a Vitrobot Mark IV (Thermo Scientific). The sample was blotted in a chamber at 4 °C and 100% humidity for 6 s at 0 blotting force before being freezing in liquid ethane.

Samples were imaged on a Titan Krios G3i 300 kV electron microscope with a Gatan K3 direct electron detector. 40–42 frame movies were collected with a nominal dose of 41–43 $e^-/Å^2$. Super-resolution images for all datasets were collected at ×105,000 magnification with a pixel size of 0.415 Å/pixel.

Data processing

Two datasets of 5427 (DSA) and 4736 (DSB) movies were collected and processed in cryoSPARC v4.4.1[58,59]. Movies were patch motion corrected with a Fourier-crop factor of 0.5 and an alignment resolution of 3 Å, followed by the patch CTF estimation. Micrographs were manually curated based on a maximum CTF fit resolution of 8 Å. The template for autopicking were created with 94,896 (DSA) and 94,858 (DSB) particles blob picked from subsets of 300 micrographs from each dataset and used for extraction. 1,281,269 and 1,491,899 particles were extracted and binned by a factor of 4 with a box size of 72 pixels from DSA and DSB, respectively. These particles were 2D classified with 100 classes, resulting in 360,885 (DSA) and 225,211 (DSB) good particles that were re-extracted. A three-class heterogeneous refinement was performed to separate good particles with the TRPV5 apo map (EMD-25716 [https://www.ebi.ac.uk/emdb/EMD-25716]) as a reference, resulting in a good class of 233,564 (DSA) and 160,664 (DSB) particles at 0.83 and 1.66 Å/pix, respectively. Particles were refined with a non-uniform refinement with no symmetry to generate the initial model[12]. Particles from DSA were subjected to 3D classification with 5 classes focusing on the pore region. The best class, totaling 57,516 particles, were combined to produce a map with a resolution of 3.53 Å with no symmetry at 0.83 Å/pix. These particles were subjected to two rounds of heterogeneous refinement and non-uniform refinement, resulting in 33,086 particles, which produced a structure with a resolution of 3.44 Å. Similarly, 22,633 particles were obtained from DSB after subjected to two rounds of heterogeneous refinement and non-uniform refinement: these particles generated a structure with a resolution of 3.83 Å. Both datasets were combined and heterogeneously refined into three volumes. The best structure form with 42.348 particles was refined with a non-uniform refinement to produce the final map with a resolution of 3.37 Å with no symmetry.

The local resolution was determined in cryoSPARC, and the angular distributions were generated with the UCSF pyem package.

Model building

The $TRPV5_{PIP2}$ model (8FFO) (Lee et al.[17]) was used as the initial model and manually adjusted in ISOLDE[60]. Lipids, PI(4,5)P_2 (PIO), and Menthol

(IT9), obtained from the ePDB database, were docked and manually adjusted in COOT[61]. Real Space_Refinement and eLBOW from the PHENIX software[62] were used to refine and to generate ligand restraints, respectively.

Pore profiles were determined using HOLE[17,63]. Chimera, ChimeraX, and PyMol were used for analysis, visualization, and figure generation.

Molecular dynamics simulations

The $TRPV5_{PIP_2}$ coordinate model (PDB ID: 8FFO) (Lee et al.[17]), oriented using the 6DMU structure from the Positioning of Proteins in Membranes (OPM) server (http://opm.phar.umich.edu/server.php), was embedded in a 1-palmitoyl-2-oleoyl-sn-glycerol-3-phosphocholine (POPC) lipid bilayer (606 molecules) along with phosphatidylinositol-4,5-bisphosphate (model with PIO, 4 molecules) and ergosterol (8 molecules) at pH 7.3. The protein-membrane complex was solvated with TIP3 water, 100 mM NaCl, and approximately 8 mM menthol, resulting in a system containing 84,087 water molecules, 203 Na^+, 151 Cl^-, and 20 menthol molecules within a $160 \times 160 \times 160$ Å^3 simulation box (Supplementary Table 4). The membrane-protein system was built using the CHARMM-GUI membrane builder[64] (http://www.charmm-gui.org). The topologies for menthol and PIO were generated using CGenFF server (https://cgenff.com, Supplementary information), then converted from CHARMM CGenFF toppar stream files to GROMACS format using cgenff_charmm2gmx_py3_nx2.py (https://mackerell.umaryland.edu/charmm_ff.shtml) together with the charmm36-jul2022.ff force field (https://mackerell.umaryland.edu/charmm_ff.shtml). Menthol molecules were placed randomly in the aqueous region.

Molecular dynamics (MD) simulations were performed using the GPU-accelerated GROMACS 2024.3[65] package with the CHARMM36m force field[66]. The system was energy-minimized and equilibrated using the steepest descent algorithm in CHARMM-GUI without modifications in configuration files (Supplementary information). In the final equilibration step, the system remained stable with a total energy of $-2.75 \times 10^6 \pm 691.63$ kJ/mol, where the potential energy was $-3.76 \times 10^6 \pm 1340.85$ kJ/mol and the kinetic energy was $1.01 \times 10^6 \pm 1171.37$ kJ/mol. The temperature remained at 303.18 ± 0.35 K, and the volume at 3631.97 ± 1.17 nm^3. The protein RMSD remained at 0.058 ± 0.008 nm. The temperature was maintained at 303 K using a Nosé–Hoover thermostat, and the pressure at 1 bar using a Parrinello–Rahman barostat. Bond constraints were applied using the LINCS algorithm. Long-range electrostatic interactions were calculated using the Particle Mesh Ewald (PME) method with a 12 Å cutoff and updated every 2 fs. Van der Waals interactions were switched at 10 Å with a 12 Å cutoff. Production simulations consisted of four independent 500 ns runs at 0 mV membrane voltage, and trajectory analyses were performed using GROMACS tools and VMD.

Molecular docking

Docking of menthol into the cryoEM structure was carried out with AutoDock Vina implemented in SwisDock[67]. We used a box of $18 \times 18 \times 8$ Å comprising the position of W583. Default parameters were used with an exhaustivity of 64.

Reporting summary

Further information on research design is available in the Nature Portfolio Reporting Summary linked to this article.

Data availability

All cryo-EM data generated in these studies are available upon request from Vera Y. Moiseenkova-Bell (vmb@pennmedicine.upenn.edu). The cryo-EM maps have been deposited in the Electron Microscopy Data Bank (EMDB) under accession code EMD-70173 ($TRPV5_{PIP2+Menthol}$); EMD-25716 ($TRPV5_{Apo}$); EMD-29049 ($TRPV5_{PIP2}$). The atomic coordinates have been deposited in the Protein Data Bank (PDB) under accession code 9O6G ($TRPV5_{PIP2+Menthol}$); 8TF2 ($TRPV5_{Apo}$): 8FFO ($TRPV5_{PIP2}$). All molecular dynamics trajectories can be accessed on Zenodo[68]. All other data is included in the paper. Source data are provided with this paper.

References

1. Gunthorpe, M. J., Benham, C. D., Randall, A. & Davis, J. B. The diversity in the vanilloid (TRPV) receptor family of ion channels. *Trends Pharmacol. Sci.* **23**, 183–191 (2002).
2. Yue, L., Peng, J.-B., Hediger, M. A. & Clapham, D. E. CaT1 manifests the pore properties of the calcium-release-activated calcium channel. *Nature* **410**, 705–709 (2001).
3. Nilius, B. et al. Whole-cell and single channel monovalent cation currents through the novel rabbit epithelial Ca^{2+} channel ECaC. *J. Physiol.* **527**, 239–248 (2000).
4. Clapham, D. E. TRP channels as cellular sensors. *Nature* **426**, 517–524 (2003).
5. Hoenderop, J. G. J. et al. Renal Ca2+ wasting, hyperabsorption, and reduced bone thickness in mice lacking TRPV5. *J. Clin. Investig.* **112**, 1906–1914 (2003).
6. Van Der Eerden, B. C. J. et al. The epithelial Ca^{2+} channel TRPV5 is essential for proper osteoclastic bone resorption. *Proc. Natl. Acad. Sci. USA* **102**, 17507–17512 (2005).
7. Dang, S. et al. Structural insight into TRPV5 channel function and modulation. *Proc. Natl. Acad. Sci. USA* **116**, 8869–8878 (2019).
8. Pumroy, R. A., Fluck, E. C., Ahmed, T. & Moiseenkova-Bell, V. Y. Structural insights into the gating mechanisms of TRPV channels. *Cell Calcium* **87**, 102168 (2020).
9. Nilius, B. et al. The single pore residue Asp542 determines Ca2+ permeation and Mg2+ block of the epithelial Ca2+ channel. *J. Biol. Chem.* **276**, 1020–1025 (2001).
10. Vennekens, R. et al. Pore properties and ionic block of the rabbit epithelial calcium channel expressed in HEK 293 cells. *J. Physiol.* **530**, 183–191 (2001).
11. De Groot, T. et al. Molecular mechanisms of calmodulin action on TRPV5 and modulation by parathyroid hormone. *Mol. Cell. Biol.* **31**, 2845–2853 (2011).
12. Hughes, T. E. T. et al. Structural insights on TRPV5 gating by endogenous modulators. *Nat. Commun.* **9**, 4198 (2018).
13. Zuidscherwoude, M. et al. Calmodulin regulates TRPV5 intracellular trafficking and plasma membrane abundance. *J. Physiol.* **602**, 6871–6888 (2024).
14. Van Der Wijst, J. et al. A gate hinge controls the epithelial calcium channel TRPV5. *Sci. Rep.* **7**, 45489 (2017).
15. Hoenderop, J. G. J. et al. Modulation of renal Ca^{2+} transport protein genes by dietary Ca^{2+} and 1,25-dihydroxyvitamin D_3 in 25hydroxyvitamin D_3 -1α-hydroxylase knockout mice. *FASEB J.* **16**, 1398–1406 (2002).
16. De Groot, T. et al. Parathyroid hormone activates TRPV5 via PKA-dependent phosphorylation. *J. Am. Soc. Nephrol.* **20**, 1693–1704 (2009).
17. Lee, B.-H., De Jesús Pérez, J. J., Moiseenkova-Bell, V. & Rohacs, T. Structural basis of the activation of TRPV5 channels by long-chain acyl-Coenzyme-A. *Nat. Commun.* **14**, 5883 (2023).
18. Cha, S.-K., Wu, T. & Huang, C.-L. Protein kinase C inhibits caveolae-mediated endocytosis of TRPV5. *Am. J. Physiol. Ren. Physiol.* **294**, F1212–F1221 (2008).
19. Chang, Q. et al. The ß-glucuronidase klotho hydrolyzes and activates the TRPV5 channel. *Science* **310**, 490–493 (2005).
20. Landowski, C. P., Bolanz, K. A., Suzuki, Y. & Hediger, M. A. Chemical inhibitors of the calcium entry channel TRPV6. *Pharm. Res.* **28**, 322–330 (2011).

21. Janssens, A. et al. Δ9-tetrahydrocannabivarin impairs epithelial calcium transport through inhibition of TRPV5 and TRPV6. *Pharmacol. Res.* **136**, 83–89 (2018).
22. Hughes, T. E. et al. Structure-based characterization of novel TRPV5 inhibitors. *eLife* **8**, e49572 (2019).
23. De Jesús-Pérez, J. J. et al. Structural mechanism of TRPV5 inhibition by econazole. *Structure* **32**, 148–156.e5 (2024).
24. Neuberger, A., Nadezhdin, K. D. & Sobolevsky, A. I. Structural mechanisms of TRPV6 inhibition by ruthenium red and econazole. *Nat. Commun.* **12**, 6284 (2021).
25. Pumroy, R. A. et al. Molecular details of ruthenium red pore block in TRPV channels. *EMBO Rep.* **25**, 506–523 (2024).
26. Bautista, D. M. et al. The menthol receptor TRPM8 is the principal detector of environmental cold. *Nature* **448**, 204–208 (2007).
27. Yang, T.-C. et al. Antiperistaltic effect and safety of l-menthol for esophagogastroduodenoscopy in the elderly with contraindication to hyoscine-N-butylbromide. *Sci. Rep.* **12**, 10418 (2022).
28. Valentovic, M., Brown, K. C. & McGuffey, E. Renal cytotoxicity of the E-vaping flavoring agent menthol. in *ASPET 2024 Annual Meeting Abstract - Toxicology* 414 (American Society for Pharmacology and Experimental Therapeutics, 2024). https://doi.org/10.1124/jpet.414.129161.
29. Macpherson, L. J. et al. More than cool: promiscuous relationships of menthol and other sensory compounds. *Mol. Cell. Neurosci.* **32**, 335–343 (2006).
30. Nguyen, T. H. D., Itoh, S. G., Okumura, H. & Tominaga, M. Structural basis for promiscuous action of monoterpenes on TRP channels. *Commun. Biol.* **4**, 293 (2021).
31. Takaishi, M. et al. Reciprocal effects of capsaicin and menthol on thermosensation through regulated activities of TRPV1 and TRPM8. *J. Physiol. Sci.* **66**, 143–155 (2016).
32. Kashio, M. et al. Involvement of TRPV4 in temperature-dependent perspiration in mice. *eLife* **13**, RP92993 (2024).
33. Anderson, C. S., MacKinnon, R., Smith, C. & Miller, C. Charybdotoxin block of single Ca2+-activated K+ channels. Effects of channel gating, voltage, and ionic strength. *J. Gen. Physiol.* **91**, 317–333 (1988).
34. Fluck, E. C., Yazici, A. T., Rohacs, T. & Moiseenkova-Bell, V. Y. Structural basis of TRPV5 regulation by physiological and pathophysiological modulators. *Cell Rep.* **39**, 110737 (2022).
35. Bhardwaj, R. et al. Inactivation-mimicking block of the epithelial calcium channel TRPV6. *Sci. Adv.* **6**, eabe1508 (2020).
36. Van Der Wijst, J., Van Goor, M. K., Schreuder, M. F. & Hoenderop, J. G. TRPV5 in renal tubular calcium handling and its potential relevance for nephrolithiasis. *Kidney Int.* **96**, 1283–1291 (2019).
37. Chen, Y. et al. Vitamin D receptor suppresses proliferation and metastasis in renal cell carcinoma cell lines via regulating the expression of the epithelial Ca2+ channel TRPV5. *PLoS ONE* **13**, e0195844 (2018).
38. Marini, M. et al. TRP channels in cancer: signaling mechanisms and translational approaches. *Biomolecules* **13**, 1557 (2023).
39. Wang, H. & Meng, F. The permeability enhancing mechanism of menthol on skin lipids: a molecular dynamics simulation study. *J. Mol. Model.* **23**, 279 (2017).
40. Yang, S. et al. A multiscale study on the penetration enhancement mechanism of menthol to osthole. *J. Chem. Inf. Model.* **56**, 2234–2242 (2016).
41. Schmitz, D., Shubert, V. A., Betz, T. & Schnell, M. Exploring the conformational landscape of menthol, menthone, and isomenthone: a microwave study. *Front. Chem.* **3**, 15 (2015).
42. Linder, T., Saxena, P., Timin, E., Hering, S. & Stary-Weinzinger, A. Structural insights into trapping and dissociation of small molecules in K^+ channels. *J. Chem. Inf. Model.* **54**, 3218–3228 (2014).
43. Zubcevic, L., Hsu, A. L., Borgnia, M. J. & Lee, S.-Y. Symmetry transitions during gating of the TRPV2 ion channel in lipid membranes. *eLife* **8**, e45779 (2019).
44. Yin, Y. et al. Visualizing structural transitions of ligand-dependent gating of the TRPM2 channel. *Nat. Commun.* **10**, 3740 (2019).
45. Chen, X., Xu, L., Zhang, H., Wen, H. & Yang, F. Differential activation of TRPM8 by the stereoisomers of menthol. *Front. Pharmacol.* **13**, 898670 (2022).
46. Yin, Y. et al. Structural basis of cooling agent and lipid sensing by the cold-activated TRPM8 channel. *Science* **363**, eaav9334 (2019).
47. Xiao, B. et al. Identification of transmembrane domain 5 as a critical molecular determinant of menthol sensitivity in mammalian TRPA1 channels. *J. Neurosci.* **28**, 9640–9651 (2008).
48. Karashima, Y. et al. Bimodal action of menthol on the transient receptor potential channel TRPA1. *J. Neurosci.* **27**, 9874–9884 (2007).
49. Umezu, T. Identification of novel target molecules of l-menthol. *Heliyon* **7**, e07329 (2021).
50. Oz, M., El Nebrisi, E. G., Yang, K.-H. S., Howarth, F. C. & Al Kury, L. T. Cellular and molecular targets of menthol actions. *Front. Pharmacol.* **8**, 472 (2017).
51. Van Goor, M. K. C., Hoenderop, J. G. J. & Van Der Wijst, J. TRP channels in calcium homeostasis: from hormonal control to structure-function relationship of TRPV5 and TRPV6. *Biochim. Biophys. Acta Mol. Cell Res.* **1864**, 883–893 (2017).
52. National Toxicology Program. Bioassay of dl-menthol for possible carcinogenicity. *Natl. Cancer Inst. Carcinog. Tech. Rep. Ser.* **98**, 1–131 (1979).
53. Wu, Y. et al. Decreased expression of the epithelial Ca^{2+} channel TRPV5 and TRPV6 in human renal cell carcinoma associated with vitamin D receptor. *J. Urol.* **186**, 2419–2425 (2011).
54. Cui, J., Bian, J.-S., Kagan, A. & McDonald, T. V. CaT1 contributes to the stores-operated calcium current in Jurkat T-lymphocytes. *J. Biol. Chem.* **277**, 47175–47183 (2002).
55. Lezin, G., Kosaka, Y., Yost, H. J., Kuehn, M. R. & Brunelli, L. A one-step miniprep for th e isolation of plasmid DNA and lambda phage particles. *PLoS ONE* **6**, e23457 (2011).
56. Colquhoun, D. & Sigworth, F. J. Fitting and statistical analysis of single-channel records. in *Single-Channel Recording* (eds Sakmann, B. & Neher, E.) 483–587 (Springer US, 1995).
57. Sigworth, F. J. & Sine, S. M. Data transformations for improved display and fitting of single-channel dwell time histograms. *Biophys. J.* **52**, 1047–1054 (1987).
58. Punjani, A., Zhang, H. & Fleet, D. J. Non-uniform refinement: adaptive regularization improves single-particle cryo-EM reconstruction. *Nat. Methods* **17**, 1214–1221 (2020).
59. Punjani, A. & Fleet, D. J. 3D variability analysis: resolving continuous flexibility and discrete heterogeneity from single particle cryo-EM. *J. Struct. Biol.* **213**, 107702 (2021).
60. Croll, T. I. *ISOLDE*: a physically realistic environment for model building into low-resolution electron-density maps. *Acta Crystallogr. Sect. Struct. Biol.* **74**, 519–530 (2018).
61. Emsley, P., Lohkamp, B., Scott, W. G. & Cowtan, K. Features and development of *Coot*. *Acta Crystallogr. D Biol. Crystallogr.* **66**, 486–501 (2010).
62. Adams, P. D. et al. *PHENIX*: a comprehensive Python-based system for macromolecular structure solution. *Acta Crystallogr. D Biol. Crystallogr.* **66**, 213–221 (2010).
63. Smart, O. S., Neduvelil, J. G., Wang, X., Wallace, B. A. & Sansom, M. S. P. HOLE: a program for the analysis of the pore dimensions of ion channel structural models. *J. Mol. Graph.* **14**, 354–360 (1996).
64. Jo, S., Kim, T., Iyer, V. G. & Im, W. CHARMM-GUI: a web-based graphical user interface for CHARMM. *J. Comput. Chem.* **29**, 1859–1865 (2008).

65. Berendsen, H. J. C., Van Der Spoel, D. & Van Drunen, R. GROMACS: a message-passing parallel molecular dynamics implementation. *Comput. Phys. Commun.* **91**, 43–56 (1995).
66. Huang, J. et al. CHARMM36m: an improved force field for folded and intrinsically disordered proteins. *Nat. Methods* **14**, 71–73 (2017).
67. Bugnon, M. et al. SwissDock 2024: major enhancements for small-molecule docking with attracting cavities and Autodock Vina. *Nucleic Acids Res.* **52**, W324–W332 (2024).
68. De Jesus-Perez, J. J. & Moiseenkova-Bell, V. MD simulation of TRPV5 in the presence of PIP2 and Menthol [Data set]. *Zenodo*. https://doi.org/10.5281/zenodo.18472580 (2026).

Acknowledgements

This work was supported by grants CF-G-513 from Consejo Nacional de Humanidades, Ciencias y Tecnologías (CONAHCYT)-Mexico and IN201824 from Dirección General de Asuntos del Personal Académico (DGAPA)-Programa de Apoyo a Proyectos de Investigación e Innovación Tecnológica (PAPIIT) to L.D.I. and Grants CBF2023-2024-46 (CONAHCYT-Mexico) and IN200423 (DGAPA-PAPIIT) to T.R. We thank Itzel Llorente for excellent technical assistance. We acknowledge the use of instruments at the Electron Microscopy Resource Lab and at the Beckman Center for Cryo-Electron Microscopy at the Institute of Structural Biology of the University of Pennsylvania Perelman School of Medicine (RRID:SCR_022375). We also thank P. Gogoi for assistance with Krios microscope operation at the University of Pennsylvania. This work was supported by grant from the National Institute of Health: Maximizing Investigators' Research Award (MIRA) (R35GM144120 to V.M.-B).

Author contributions

A.M.-R. performed electrophysiology experiments, analyzed data, wrote and edited the manuscript; J.J de J.P., performed biochemical and cryo-EM experiments, molecular dynamics simulations, analyzed data, wrote and edited the manuscript; G.E.R-Y., performed molecular biology experiments, and edited the manuscript; T.R. performed electrophysiology experiments, analyzed data, wrote and edited the manuscript; V.M-B, analyzed data, wrote and edited the manuscript; L.D.I. performed electrophysiology experiments, analyzed data, wrote and edited the manuscript.

Competing interests

The authors declare no competing interests.

Additional information

Supplementary information The online version contains supplementary material available at https://doi.org/10.1038/s41467-026-70759-8.

Correspondence and requests for materials should be addressed to Vera Moiseenkova-Bell or León D. Islas.

Peer review information *Nature Communications* thanks the anonymous reviewer(s) for their contribution to the peer review of this work. A peer review file is available.

Reprints and permissions information is available at http://www.nature.com/reprints

Publisher's note Springer Nature remains neutral with regard to jurisdictional claims in published maps and institutional affiliations.

Open Access This article is licensed under a Creative Commons Attribution-NonCommercial-NoDerivatives 4.0 International License, which permits any non-commercial use, sharing, distribution and reproduction in any medium or format, as long as you give appropriate credit to the original author(s) and the source, provide a link to the Creative Commons licence, and indicate if you modified the licensed material. You do not have permission under this licence to share adapted material derived from this article or parts of it. The images or other third party material in this article are included in the article's Creative Commons licence, unless indicated otherwise in a credit line to the material. If material is not included in the article's Creative Commons licence and your intended use is not permitted by statutory regulation or exceeds the permitted use, you will need to obtain permission directly from the copyright holder. To view a copy of this licence, visit http://creativecommons.org/licenses/by-nc-nd/4.0/.

© The Author(s) 2026